Multiple-photon peak generation near the ~10 μm range in quantum dot infrared photodetectors

Marcos H. Degani, Marcelo Z. Maialle, Paulo F. Farinas, Nelson Studart, Mauricio P. Pires, and Patricia L. Souza

Citation: Journal of Applied Physics **109**, 064510 (2011); doi: 10.1063/1.3556432
View online: http://dx.doi.org/10.1063/1.3556432
View Table of Contents: http://scitation.aip.org/content/aip/journal/jap/109/6?ver=pdfcov
Published by the AIP Publishing

Multiple-photon peak generation near the ~10 μm range in quantum dot infrared photodetectors

Marcos H. Degani,[1,a)] Marcelo Z. Maialle,[1] Paulo F. Farinas,[2,b)] Nelson Studart,[2] Mauricio P. Pires,[3] and Patricia L. Souza[4]
[1]*Faculdade de Ciências Aplicadas, Universidade Estadual de Campinas, 13484-350, Limeira, SP, Brazil and DISSE - Instituto Nacional de Ciência e Tecnologia de Dispositivos Semicondutores, CNPq/MCT, Brazil*
[2]*Departamento de Física, Universidade Federal de São Carlos, 13565-905, São Carlos, SP, Brazil and DISSE - Instituto Nacional de Ciência e Tecnologia de Dispositivos Semicondutores, CNPq/MCT, Brazil*
[3]*Instituto de Física, Universidade Federal do Rio de Janeiro, 21645-970, Rio de Janeiro, RJ, Brazil and DISSE - Instituto Nacional de Ciência e Tecnologia de Dispositivos Semicondutores, CNPq/MCT, Brazil*
[4]*LabSem/CETUC, Pontifícia Universidade Católica, Rio de Janeiro, RJ 22451-900, Brazil and DISSE - Instituto Nacional de Ciência e Tecnologia de Dispositivos Semicondutores, CNPq/MCT, Brazil*

(Received 5 December 2010; accepted 17 January 2011; published online 22 March 2011)

We present results from simulations of the photocurrent observed in recently fabricated InAs quantum dot infrared photodetectors that respond with strong resonance peaks in the ~10 μm wavelength range. The results are in good agreement with experimental data generated earlier. Multiphoton scattering of electrons localized in the quantum dots are not only in accordance with the observed patterns, but are also necessary to explain the photocurrent spectrum obtained in the calculations. © *2011 American Institute of Physics*. [doi:10.1063/1.3556432]

I. INTRODUCTION

For many years now, mid-infrared photodetection has consistently been an issue of interest in various research fields.[1] Infrared photodetectors fabricated with self-assembled grown quantum dots (QDIPs) in III-V based structures, instead of quantum well heterojunctions (QWIPs), have become promising thanks to their varying peculiar characteristics.[2,3] Some of the advantages of QDIPs over QWIPs arise from the following properties[4]: (1) S-polarized light can couple more efficiently to charge carriers in the QDIPs yielding stronger coupling with the normal incident light while in the QWIPs the light must be shed with at least some component transverse to the normal (growth) direction. In a QWIP, electrons behave as if they were free in the direction perpendicular to the normal, so that the electric field component in that direction can only shift the unperturbed levels, producing no coupling between them; (2) improved precision of the absorption resonances follow from the narrow linewidths of the well defined atomiclike energy levels; (3) fewer constraints when designing multicolor devices, as one can, for example, combine modules of different dot sizes; (4) lower dark currents are expected, as a consequence of the longer relaxation times, typical in the much smaller size confinement of QDIP structures; (5) potential for larger gains, achieved in the III-V QDIPs due to the less effective recombination of charge carriers as compared to QWIPs; (6) sharper linewidths and strongly localized states mediating the emission processes, which are thought to improve the operation of the QDIPs at higher temperatures as compared to QWIPs.[5,6]

InAs quantum dot structures grown on InGaAlAs have been experimentally investigated in Refs. 12 and 13 for mid-infrared photodetection. In this work we review some of these measurements of photocurrent in QDIP in light of new theoretical results. As it will be recalled, the existence of the peaks experimentally observed cannot be understood by considering only the inherent single-photon processes in the structures. It has been conjectured in Ref. 13 that higher order processes due to electron-electron interactions, specifically the Auger scattering, might be responsible for the appearance of the peaks. We see here, however, by using a single-electron model, that it is possible to reproduce the observed photocurrent peaks and all their main trends, leading to an alternative explanation in terms of multiple photon processes.

Reference to multiple photon processes has become common in the recent literature in order to understand the optical responses of infrared devices, and experimental evidence that they occur in these devices has been gathering now for a while, together with theoretical approaches to explain them.[7–10]

Multi-photon processes may differ in their nature, in the sense that photons can either be absorbed simultaneously or in sequential scattering events. As we will see, the transitions that come out of the single-electron calculations presented here are due to sequential processes, with the electrons being photoexcited out of the dot via multi-photon transitions (bound to continuum transitions).

The transitions generating the photocurrent are strongly enhanced by the presence of intermediate energy levels in sequential photon absorptions. This process is conceptually similar to multiphoton ionization of an atom, however, the dipole matrices in the semiconductor system we investigated are considerably larger.[11] This allows for the multi-photon resonance channels to contribute in the photoexcitation of

a)Electronic mail: mhdegani@hotmail.com.
b)On leave from Instituto de Física, Universidade Federal do Rio de Janeiro, Rio de Janeiro, RJ, Brazil.

electrons for the relatively low intensity light sources used to generate the experimental plots presented at the top of Fig. 2.

II. PRELIMINARY DISCUSSION OF THE SYSTEM AND THE RESULTS

In this Section, we briefly describe the system studied and anticipate the main aspects of the new results obtained in our calculations and compare them to the results of early measurements. Additional details about both the system's structure and the experimental results have been presented in Refs. 12 and 13.

The representation of the system investigated is shown in Fig. 1. The dots are lens shaped self-assembled structures that protrude from a wetting layer, as schematically shown in the figure.

Our calculations were carried for both coin-shaped dots (as illustrated in Fig. 1) and lens-shaped dots. In the latter case, the shape was adjusted to follow regular patterns obtained in micrography images taken from the dots. Such a difference in the shape of the dots yielded no relevant changes in the final simulation results, although the energy structure was of course rearranged for different geometries. As we will see, the electron multi-scattering processes that generate the photocurrent involve the excitation of electrons from low lying states localized inside the dot up to a state in the continuum, with absorption of a few photons, so that the tens of intermediate states in between the ones involved do not play a major role.

In Fig. 2, we see curves extracted from experimental observations (at the top plot) together with some of the simulated results. As we will see in the next Section, the quantum dots are modeled as potential-barrier structures, and a single electron, subjected to an external oscillating electric field, is used to obtain the results of the calculations. The polarization of such a field is made perpendicular to the z direction (see Fig. 1) to represent the real experimental situation regarding the (normal) incidence of the photons. In addition, a static electric field (F_z, disclosed in the labels of Fig. 2) is considered along the z direction. We are not able to track down the quantitative correspondence between the exact values of the real electric fields acting upon the electron inside the samples. The reason for this is the existence of intrinsic fields in the samples that are unknown. However, the order of magnitudes are in correspondence as well as the behavior obtained by varying F_z, in remarkable agreement, as seen in Fig. 2.

III. THEORETICAL APPROACH FOR THE SIMULATIONS

We would like to state up front that the reader who becomes interested in deeper theoretical details than what is presented here is very encouraged to refer to Ref. 15. Technical details like boundary conditions, continuous versus discrete states, conservative versus nonconservative systems, and others, are quite traditionally handled, and are explained in both Ref. 15 and in the references therein, which form an important part of the wide literature about these techniques.

An effective Hamiltonian for a single electron interacting with an external oscillating electric field is used to run the numerical simulations,

$$\mathcal{H} = -\frac{\hbar^2}{2m^*}\nabla^2 + V(r) - ezF_z - exA(t)\sin\omega t, \qquad (1)$$

where m^* is the electron effective mass, assumed uniform throughout the system, $V(r)$ is the potential due to the quantum dot structure, whose profile is shown in the right-hand-side of Fig. 1, $A(t)$ is the envelope amplitude of the

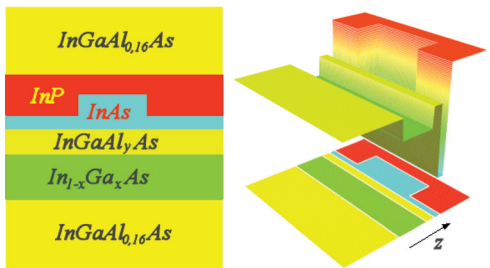

FIG. 1. (Color online) Representation of the quantum dot structure studied. The left panel illustrates the layers along the growth (z) axis. The structure is cylindrically symmetrical around z. The right panel shows a 3D plot of the potential: the vertical axis shows the potential energy while the other axis perpendicular to z can be any of the infinitely many equivalent directions passing through the center of the dot. The precise locus of the origin along z is shown in Fig. 3.

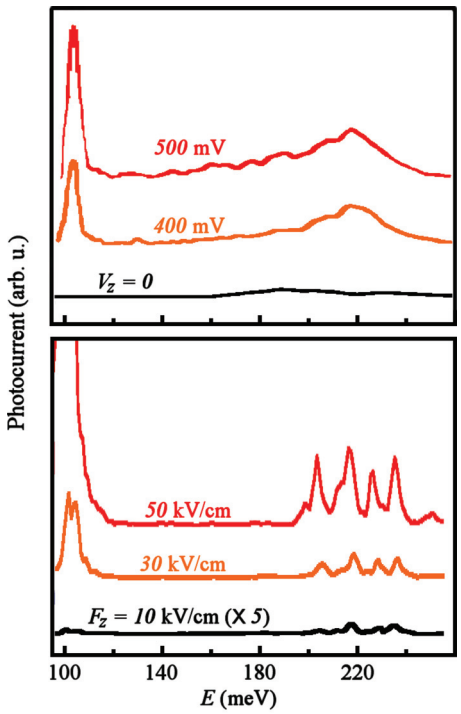

FIG. 2. (Color online) Comparison between experimental (at the top) and calculated values for the photocurrent. The curves in either graph are not in direct correspondence regarding the static electric fields indicated. The overall trends in the simulated results come out in good agreement with the experiments despite the simplicity of the single-electron model used. Both experimental and calculated curves are obtained for s-wave (normally incident) light shed on the structure.

oscillating field, and F_z is the intensity of the static field. The time-varying field interacts with the quantum structure, and the resulting absorbtions at specific frequencies (ω) give the resonance channels for photons of energy $\hbar\omega$ to be captured. Hence, the spectral plots presented here are generated by performing calculations for different values of ω.

Band offsets due to the matching of the grown layers and the self assembled dot were taken from Ref. 12, where the existence of strains in the dot were accounted for by following the general ideas described in Ref. 14. The envelope is taken in the form of a pulse, with Gaussian or some other short living form used to excite the system. The results are not very sensitive to the form chosen. The ground state of the system is calculated first by setting $A(t) \equiv 0$. The resulting ground-state wave function is used as $\psi(0)$, the state of the system at $t = 0$, when the oscillating pulse is turned on, and the full Hamiltonian in Eq. (1) (with $A(t) \neq 0$) is used to numerically evolve the system in time to obtain $\psi(t)$. A time-dependent current density is then calculated by adding the outgoing components of the current-flux,

$$\boldsymbol{J}(\boldsymbol{x}, \boldsymbol{y}, \boldsymbol{t}) = \sum_{z_0} \mathrm{Re}\left[\frac{\hbar}{\boldsymbol{i}\boldsymbol{m}^*}\psi(\boldsymbol{r}, \boldsymbol{t})^* \nabla\psi(\boldsymbol{r}, \boldsymbol{t})\right]_{z=z_0}, \qquad (2)$$

from which the integrated current is taken,

$$I = \int \hat{z} \cdot \boldsymbol{J}(\boldsymbol{x}, \boldsymbol{y}, \boldsymbol{t})\boldsymbol{dxdydt}, \qquad (3)$$

in arbitrary units. The value of z_0 is chosen at two locations far away from the dot in the z axis so that the above sum has two terms, corresponding to outgoing contributions in the directions $\pm z$.

In order to implement the algorithm just outlined, we numerically solve Schrodinger's Equation by using the method of the split-operator.[15–18] This method consists of propagating the wave function from a given initial state $\psi(t)$ to $\psi(t + \Delta t)$ through the usual unitary propagator

$$U(t, t + \Delta t) = \exp\left[\frac{-i}{\hbar}\int_t^{t+\Delta t} dt' \mathcal{H}(t')\right], \qquad (4)$$

by splitting U into the product $U_{pot}U_{kin}U_{pot}$, where the new operators contain only potential (kinetic) parts of $\mathcal{H}$. Such a splitting introduces an error of order of some power of Δt, due to the noncommuting nature of the potential and kinetic operators. There is a compromise between the power of Δt obtained in a particular choice of splitting and the number of numerical steps necessary to find the solution. It is possible to keep an error of the order of Δt^3 with a considerably low number of steps. Then, by choosing a conveniently dense time-grid, the propagation of ψ is achieved with an arbitrarily small error. This yields arbitrarily precise outputs and a very quick convergence for the time evolution of ψ.

We want to note here, that this method yields the photocurrent with no need of any information about the energy spectrum or eigenstates of the system but one single initial state (presently chosen to be the ground state) which is used as the state vector at $t = 0$. In this regard, the photocurrent results (as the one shown in the lower panel of Fig. 2) are fully simulated, in the sense that one evolves a Hamiltonian in time, in a conveniently thought out manner, and then obtains information from the results.

To unveil the physics beneath the simulation, we want to relate the photocurrent results to the detailed characteristics of the structure. The method of the split-operator is also advantageous for this purpose, since it quickly obtains the ground state and from this it constructs the excited states, as outlined in what follows. In order to obtain the eigenstates of a time-independent Hamiltonian, the evolution is performed in the imaginary-time domain: From *any* trial wave function, few steps yield convergence to the ground state; one then repeats the program but now a Gram-Schmidt orthogonalization constraint drives the evolution path to the first excited state; repetition gives as many excited states as one chooses to calculate.[15]

Thus, the method allows us to calculate the eigenstates of the system exactly, one by one, while finding the spectrum without more than an educated guess of the initial ground state. The calculations are carried without the necessity of going through usual limiting issues like truncation and/or adequacy of a given basis.

IV. ANALYSIS OF THE RESULTS

As we have just noticed in the last Section, the calculated photocurrent obtained here is the direct output from the propagation in time of a given Hamiltonian [presently given by $\mathcal{H}$ in Eq. (1)], which is the representation of the system studied. All effects of such a system are automatically included in the simulation, and no access is needed to the spectrum or its properties (like, e.g, selection rules or spectral weights) in order to obtain the photocurrent. Rather it is the calculated photocurrent itself that gives us access to the resonances in the model system. From this perspective, the oscillating electromagnetic field, given by the last term of Eq. (1), works as a probe and we can understand the outcome as resulting from the scattering of the electromagnetic field by the quantum structure given in Fig. 1 and modeled in the remaining terms of $\mathcal{H}$.

To understand why specific energy peaks show up in the photocurrent, and what are the physical processes involved in the absorption of light, we proceed to obtain the spectrum as outlined in the end of the last Section. The cross-sectional z-profile of the potential barriers is illustrated in Fig. 3 to help with the subsequent analysis (we stress, however, that the full three-dimensional (3D) potential of the quantum dot structure of Fig. 1 is used to obtain all the results presented in this article). Figure 3 shows a quantum well placed to the left, while the deeper well on the right (which is crossed by the ground-state energy line) is a cross-sectional representation of the dot.

In Fig. 4, we see the average position along the z axis calculated for states up to the continuum. These positions follow in the vicinity of the wave functions' maxima, in particular for the lower energy states, which are localized in-dot states. As the energy increases, we notice from Figs. 3 and 4 that the states become more numerous and closer in energy and that for energies greater than that of the bottom of the

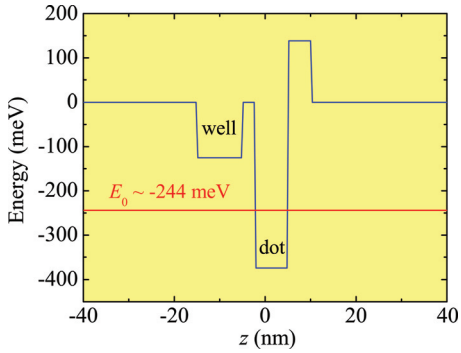

FIG. 3. (Color online) Potential barriers in the z direction in a cross-sectioned region of the structure shown in Fig. 1. The ground state energy is shown (E_0). Band offsets taken from Ref. 12, where the strains in the dot were included as in Ref. 14.

well the states become peaked inside the well. As we argue ahead, these well states serve as intermediate states in the absorption process.

In order to plot the energy spectrum, we use the following density of states (DOS),

$$\mathrm{DOS(E)} \equiv \mathrm{A}\sum_{\mathrm{n}} \mathrm{e}^{-[(\mathrm{E}-\epsilon_{\mathrm{n}})/\Delta]^2}, \tag{5}$$

given in arbitrary units, where Δ is a small artificial broadening energy to make the peaks resolved. Here, ε_n are the eigenvalues, calculated as explained in the last Section, and the normalization constant A is determined by the condition

$$\int \mathrm{DOS(E)dE} = 1. \tag{6}$$

The DOS is shown in Fig. 5 for states up to the continuum. The ground state has its energy about -240 meV, so that if the electron in the ground state absorbs one single photon with $\hbar\omega \geq 240$ meV, it could be excited to the continuum and contribute to the photocurrent.

However, the measured photocurrent spectrum, shown in Fig. 2, shows two relatively broad peaks that the simulations suggest to be a group of peaks smeared out by the ~7 K thermal bath present in the experiments (and absent in the photocurrent calculations). These peaks have been produced

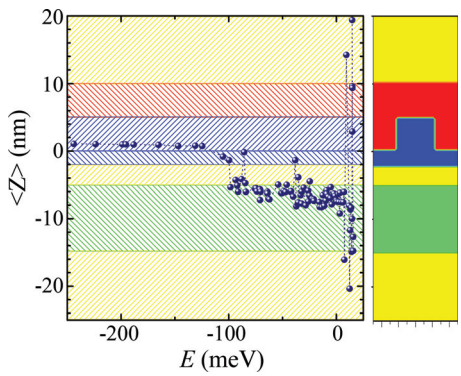

FIG. 4. (Color online) Calculated $\langle z \rangle$ for states up to the continuum and superimposed on a projection of the physical structure showing the locations of the dot and the various layers (dashed lines added for guidance).

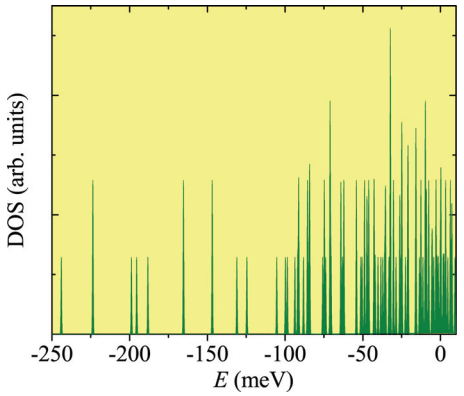

FIG. 5. (Color online) Density of states for states up to the continuum, calculated for the structure in the absence of both static and oscillating fields.

by scattering events whose energies lie out of the window of $\hbar\omega \geq 240$ meV just described, having their maxima at energies of about 100 and 200 meV. The only possibility for a single-electron Hamiltonian to reproduce them, as the one used here does, is through multiphoton absorptions.

Indeed, careful examination of the DOS plotted in Fig. 5 suggests that the ~200 meV peaks could arise from 2-photon absorptions while the ~100 meV peaks from 3-photon absorptions.

The analysis made up until now suggests that multiphoton processes have a main contribution in the generation of the photocurrent for the two peaks observed at energies less than the continuum. This analysis is not suitable if one wishes to understand why these peaks occur at the specific energies observed, i.e., the role that specific states have in order to set the selectivity shown in the experiments. In the next Section, we further understand these aspects and strengthen our proposition that multiphoton processes are the main reason for the phenomena observed.

V. PROBING THE 3D STRUCTURE

The method of the split-operator described in Sec. III can be used to probe the three-dimensional structure shown in Fig. 1 in order to reveal more details related to its spectrum. The idea consists of three complementary methods.

The general idea is to calculate time-correlation functions when probing the structure with different field polarizations, so we can check for the system's specific responses and selection rules. For our purposes it suffices to use the two first monopole (power spectrum) and dipole (absorption) moments. The reason why these two time-correlation functions will show different behaviors when the system is probed with symmetrically different fields is the anisotropy of the structure: the potential energy along the growth axis (z) is very different from that along any of the equivalent directions perpendicular to z.

A. Power spectrum

We calculate the power spectrum $P(\omega)$ by first tilting the static structure with a constant electric field applied in either the z or x directions and obtaining the ground state of the resulting static system. This is the $t < 0$ part of the

calculation. Then, at $t = 0$, the field is abruptly turned off and the $t < 0$ ground state is propagated to positive times. These calculations are done by using the numerical steps described in Sec. III. The power spectrum is then directly obtained from the Fourier transform of the time-correlation function $\langle\psi(r, 0_-)|\psi(r, t > 0)\rangle$,

$$P(\omega) \equiv \int_0^\infty dt e^{i\omega t}\langle\psi(r, 0_-)|\psi(r, t > 0)\rangle. \quad (7)$$

The split-operator method calculates this time-correlation function directly from the wave functions obtained at different times and then the result is Fourier-transformed.

Here, the purpose of tilting the structure with an external electric field is to guarantee a $t < 0$ solution that will have large enough projections in all eigenstates of the unperturbed structure yielding the whole unperturbed spectrum to show in the time-correlation function of Eq. (7). Applying the constant electric field in the x and z directions also warrants that the complete spectrum is obtained regarding both the longitudinal (z) and transverse (x) quantizations present in the 3D structure. The final spectrum is the combination of two curves obtained by using the field in both directions, as shown in Fig. 6.

The responses obtained for the two different directions in which the constant fields are applied are related, as we see in the next subsection, to the longitudinal (x) and transverse (z) polarizations of the light that can be shed on the sample. Here we also refer to these two branches of the spectrum as s -wave and p -wave, for the x and z responses, respectively.

It becomes clear that $P(\omega)$ indeed gives information about the spectrum if we write the general-solution state in the basis of the eigenstates of the unperturbed structure,

$$|\psi(r, t)\rangle = \sum_n e^{-i\epsilon_n t/\hbar} a_n |n\rangle, \quad (8)$$

where ε_n are the energy eigenvalues of the unperturbed system. As it has already been stressed, our calculations do not require the use of basis states, so such an expansion is written here only as an auxiliary statement. From Eqs. (8) and (7) we immediately see that

$$P(\omega) = \sum_n |a_n|^2 \delta(\omega - \epsilon_n), \quad (9)$$

which is clearly peaked at the eigenenergies.

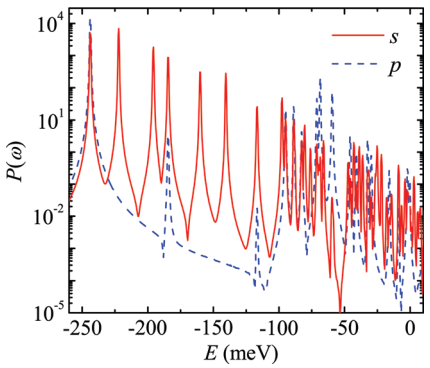

FIG. 6. (Color online) Power spectrum plotted for both transverse (s) and longitudinal (p) responses.

B. Absorption spectrum

To calculate the absorption, we use the split-operator method to solve for optical relations whose basic derivations can be appreciated in Refs. 19 and 20. We proceed as in the calculation of $P(\omega)$ in the last subsection, however we use a different time-correlation function. The absorption is taken from the Fourier transform of

$$\langle n|e^{i\mathcal{H}t/\hbar}(-ex_i)|\psi(r, t > 0)\rangle,$$

where x_i is any one of the three position observables. This correlation is the dipole moment averaged between the time-evolved eigenstate one chooses to study and the full state of the system. In the present case, we are investigating the ground state, and the absorption will be given by[19,20]

$$\alpha_i(\omega) \propto \omega \mathrm{Re}\left[\int_0^\infty \mathrm{dt}\ \mathrm{e}^{\mathrm{i}(\hbar\omega+\epsilon_0)\mathrm{t}/\hbar}\langle 0|\mathrm{x_i}|\psi(\mathrm{r}, \mathrm{t})\rangle\right]. \quad (10)$$

Again, we state that the split-operator method used here yields directly the time-correlation function in Eq. (10), without the need to find the eigenstates (except for the ground state in the case of the absorption).

If, nonetheless, we carry on an analysis similar to that of the last subsection, using Eq. (8) to check the physical content of $\alpha_i(\omega)$, the resulting expression is written, in terms of a basis set, as

$$\alpha_i(\omega) \propto \omega \mathrm{Re}\left[\sum_\mathrm{n} \mathrm{a_n}\langle 0|\mathrm{x_i}|\mathrm{n}\rangle \int_0^\infty \mathrm{dt}\ \mathrm{e}^{\mathrm{i}[\omega-(\epsilon_\mathrm{n}-\epsilon_0)/\hbar]\mathrm{t}}\right], \quad (11)$$

where a small positive imaginary part is included in the exponent's frequency to resolve the peaks. It is clear from this expression that the absorption provides information about the energy differences as measured from a reference state (which in the present case is chosen to be the ground state), and that it also accounts for dipole-moment selection rules through the matrix elements that appear in the sum.

Figure 7 depicts the absorption spectrum plotted together with the power spectrum. The solid-red and dashed-

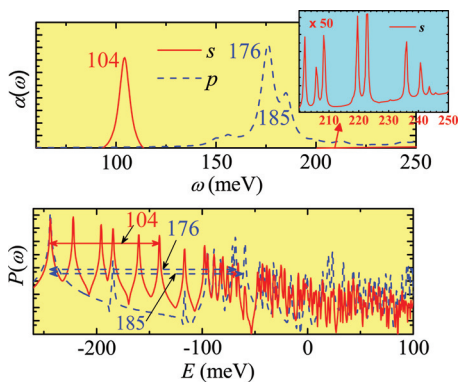

FIG. 7. (Color online) Absorption plotted on top of the energy spectrum and the associated symmetries (s and p-wave). The numbers near the peaks correspond to the exact values of the peak energies. The bottom plot is the same graph as the one shown in Fig. 6, but now depicting some of the lower transitions that are consistent with the absorption amplitudes. The inset shows that there is a cluster of peaks ~200 meV with lesser intensity and slightly greater energies in the s-wave curve.

blue curves refer to $i = x$ and $i = z$, respectively. In this figure, it becomes clear that the strength of the possible transitions are very large in the vicinity of the energies experimentally observed, which correspond to about 100 meV and 200 meV photons. However, as we see in the next subsection, the symmetries associated with the red and blue lines in Fig. 7 correspond, respectively, to the *s*-wave and *p*-wave polarizations of the incident field.

The experimental curves presented here have been obtained at 7 K, using *s*-wave polarization for the light shed on the sample, that is, the oscillating field, as well as the calculated photocurrent in Fig. 2. The lower intensity of the *s*-wave absorption, as shown in the inset of Fig. 7 explains the relative intensity of the experimentally observed peaks.

As a general feature, we note also that the ground state is the only low-lying state that combines both *s* and *p*-wave symmetries, so that one might ask what would be the relative contribution of the first excited state, lying ~22 meV (almost room temperature) above the ground state, if it turns out to be initially occupied.

C. Probing for different light polarizations

To answer to questions like the one just posed and to complete a thoroughly theoretical study of the system presented, we calculate the photocurrent by applying the oscillating field in the *z* direction. We recall that both the experimental and the calculated photocurrents shown in Sec. II correspond to light shed normally on the dot, which means the oscillating field in the *x* direction. Applying the oscillating field in different directions is accomplished by interchanging *x* with the proper observable in Eq. (1), and then calculating the photocurrent as described in Sec. III. We will use the operator *z*, which corresponds to the sample's growth direction, and since we can independently choose the oscillation amplitude in either case, we will refer to these amplitudes by A_x and A_z, respectively.

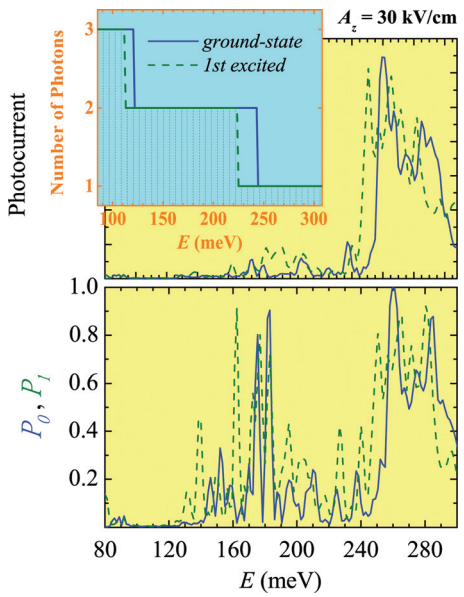

FIG. 8. (Color online) Photocurrent, in arbitrary units (top), and the ionization probability (bottom) for the *p*-wave polarization (oscillating field in the *z* (growth) direction, whose amplitude A_z is shown). The inset shows the number of photons absorbed for different energy ranges. The static bias field is zero for these curves.

Another quantity of interest we also obtain is the ionization probability, defined as

$$P_n(t) = 1 - |\langle n|\psi(r, t)\rangle|^2, \tag{12}$$

for $|\psi(r,0)\rangle \equiv |n\rangle$. This quantity has a variable value $0 \le P_n(t) \le 1$ and it is computed when a steady-state photocurrent is reached, when we denote its value by $P_n \equiv P_n(t \to \infty)$. It clearly tells us whether, at a given time $t > 0$, the steady state vector has any projection left on its initial value, chosen to be an eigenstate. Thus it will be as close to its maximum value of one as the event of the electron leaving the chosen eigenstate is more likely to occur for times greater than the transient.

We see in Fig. 8 the photocurrent calculated for a *p* polarized light shed on the system (top plot) together with the ionization probabilities P_0 and P_1 (bottom plot), for both the ground and first excited states, and for the static bias field set to zero. For this polarization, the photocurrent excited by multiple photons through states of negative energies is small as compared to the values generated by single-photon absorptions directly into the continuum, as it may be seen with help of the inset graph. The ionization probability reveals that there are resonances for energies near 200 meV, however, except for a couple of peaks, they are quite attenuated relative to the ones that correspond to the continuum, $E \ge 250$ meV. In the case of the ~100 meV region, the resonances are strongly suppressed. This is consistent with the absorption results, shown in Fig. 9 for a wider set of energy differences.

For the *p*-wave polarization there is practically no absorption near the 100 meV region. The photocurrent produced by the *p*-wave light in this region can be seen not to be exactly vanishing if we re-scale the top plot of Fig. 8 in that energy range, as shown in Fig. 10.

The opposite behavior is observed in the 100 meV region for the *s*-wave-polarization photocurrent, as we see in Fig. 11. It is clear that the strong ionization probability, sharply placed about 100 meV, leads to the strong peak observed in the photocurrent. We can also note, in the left inset of Fig. 11, the role that the static bias field plays for the existence of the 100 meV peak. In the insets of Fig. 11 it is also clear that although the ionization probability is quite

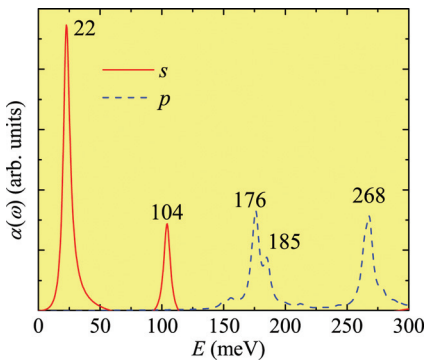

FIG. 9. (Color online) Absorption of the top plot of Fig. 7 shown over a wider energy range.

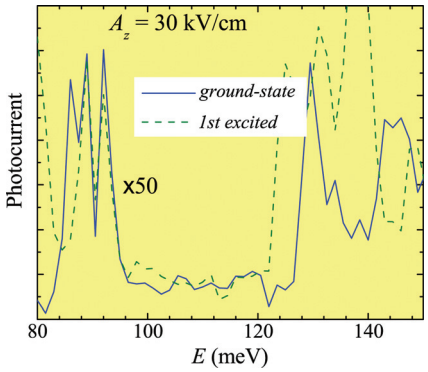

FIG. 10. (Color online) Excerpt from the top plot of Fig. 8 zoomed by 50 times in the vertical scale.

large for both zero and 50 kV/cm static biases, the photocurrent is only excited ~100 meV if the bias is nonzero.

The differences between the peak structure and bias dependence in the photocurrent and the ionization probability can be understood as follows. The ionization probability P_n defined in Eq. (12) clearly contains resonances for which a single photon is absorbed even if there are no subsequent absorptions allowed, whereas the photocurrent can only be excited if the electron is promoted up to the continuum, which can only occur, for the energies below the continuum, if multiple photons are absorbed. The existence of a peak in P_n not accompanied by a similar peak in the photocurrent indicates that one or more photons have been initially absorbed but that the electron did not reach the continuum for that energy, through subsequent necessary absorptions. Besides the selection rules of the unperturbed structure, frustration of subsequent absorptions results from the energy mismatch of available states whose energies are very sensitive to the static bias.

VI. MULTIPHOTON PROCESSES

From the structure's selectivity revealed in our calculations, we see that multiple-photon absorptions are the main physical processes leading to the observed results.

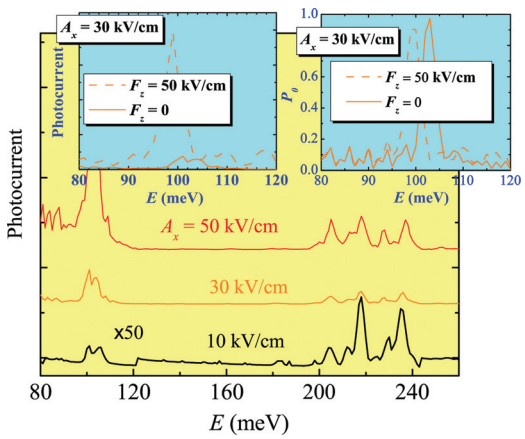

FIG. 11. (Color online) Photocurrent shown for bias static field equal to zero and various oscillating-field amplitudes for *s*-wave light. The left inset photocurrent shows the 100 meV energy region for static bias fields of both 0 and 50 kV/cm for $A_x = 30$ kV/cm. The right inset shows the ionization probability for the ground state in the same energy range and for the same oscillating field as in the left inset.

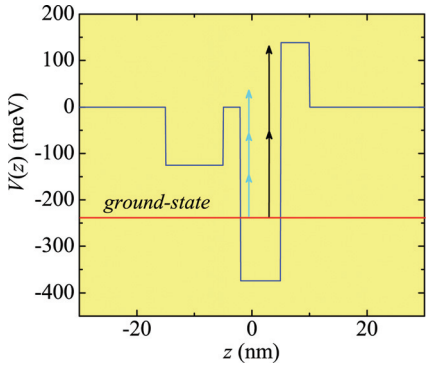

FIG. 12. (Color online) Schematic view of the multiphoton absorption processes. The electron, initially in the ground state (represented by a straight line at its energy), reaches the continuum and contributes for the photocurrent after absorbing more than one photon.

To illustrate this, we show in Figs. 12 and 13 the representative drawing of the absorption "jumps" and the energy regions that account for the different numbers of photons absorbed.

At first glance, the final transitions represented by arrows in Fig. 12 may appear somewhat arbitrary, given the existence, in the continuum, of many states for the electron to end up (see the DOS plotted in Fig. 5). However, as we see in the absorption, in the top plot of Fig. 7, the whole structure is very selective for a wide range of energies, strongly suppressing the transitions whose differences in energies are not about either 100 or 200 meV.

In Fig. 13, we see a plot of one of the photocurrent curves calculated, and shown in Fig. 2, depicted in two different scales and shown within a slightly wider energy range, which allows us to appreciate further details of the curve's structure.

VII. CONCLUSIONS

In this article, we presented a detailed theoretical study of recent experiments done with quantum dot infrared photodetectors. We presented simulations based on the split-operator method, which has various advantages as compared to other techniques, the main ones being provision of direct access to the time dependent wave function without the need

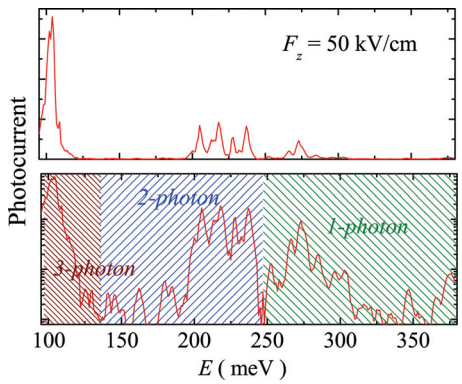

FIG. 13. (Color online) Photocurrent, in arbitrary units, shown in both linear (top) and logarithmic scales. The energy regions originating different multiphoton processes are indicated in the lower plot.

of preliminary knowledge of either the spectrum or the associated states. Slight adaptation of the method also permits one to calculate the eigenstates and eigenenergies in a very efficient manner. The results of the calculations agree well with the observed behavior. In particular, two peaks that have been experimentally observed in energy ranges for which single photon absorptions cannot provide an explanation for their existence, showed up at the same energies in our simulations. Given the simplicity of the model used in our program, the only possible processes that could account for these peaks, in this model, are multiphoton absorptions. In addition to the simulated photocurrent, we further investigated various quantities, like the density of states, both the power and absorption spectra, which build a strong case for this simple explanation in terms of multiphoton absorptions. However, scattering processes from interactions between the electronic carriers are not accounted for in our calculations, whence the importance of the multiphoton results given here relative to ones that might come from interactions (like Auger scattering), cannot be settled in this article, although it has been suggested by two of us in Ref. 13, we recall, nonetheless, that the carrier densities of the samples are quite low, which intuitively suggests that dynamical effects due to interelectronic interactions should be minimal.

ACKNOWLEDGMENTS

The authors gratefully acknowledge financial support from Programa Institutos Nacionais de Ci encia e Tecnologia and Conselho Nacional de Desenvolvimento Científico e Tecnológico - CNPq/MCT.

[1]For a recent review, see P. Martyniuk and A. Rogalski, Prog. Quantum Electron. **32**, 89 (2008).
[2]S. Chakrabarti, A. D. Stiff-Roberts, X. H. Su, P. Bhattacharya, G. Ariyawansa, and A. G. U. Perera, J. Phys. D: Appl. Phys. **38**, 2135 (2005).
[3]H. Lim, W. Zhang, S. Tsao, T. Sills, J. Szafraniec, K. Mi, B. Movaghar, and M. Razeghi, Phys. Rev. B **72**, 085332 (2005).
[4]M. Razeghi, H. Lim, S. Tsao, J. Szafraniec, W. Zhang, K. Mi and B. Movaghar, Nanotechnology **16**, 219 (2005), and references therein.
[5]D. Pal and E. Towe, Appl. Phys. Lett. **88**, 153109 (2006).
[6]P. Bhattacharya, X. H. Su, S. Chakrabarti, G. Ariyawansa, and A. G. U. Perera, Appl. Phys. Lett. **86**, 191106 (2005).
[7]E. DuPont, P. Corkum, H. C. Liu, P. H. Wilson, M. Buchanan, and Z. R. Wasilewski, Appl. Phys. Lett. **65**, 1560 (1994).
[8]T. Maier, H. Schneider, M Walther, P. Koidl, and H. C. Liu, Appl. Phys. Lett. **84**, 5162 (2004).
[9]J. Jiang, Y. Fu, N. Li, X. S. Chen, H. L. Zhen, W. Lu, M. K. Wang, X. P. Yang, G. Wu, Y. H. Fan, and Y. G. Li, Appl. Phys. Lett. **85**, 3614 (2004).
[10]P. Aivaliotis, E. A. Zibik, L. R. Wilson, J. W. Cockburn, M. Hopkinson, and N. Q. Vinh, Appl. Phys. Lett. **92**, 023501 (2008).
[11]C. Sirtori, F. Capasso, D. L. Sivco and A. Y. Cho, Appl. Phys. Lett. **60**, 2678 (1992).
[12]P. L. Souza, J. Lopes, T. Gebhard, K. Unterrainer, M. P. Pires, J. M. Villas-Boas, G. S. Vieira, P. S. S. Guimarães, and Nelson Studart, Appl. Phys. Lett. **90**, 173510 (2007).
[13]T. Gebhard, D. Alvarenga, P. L. Souza, P. S. S. Guimarães, K. Unterrainer, M. P. Pires, G. S. Vieira, and J. M. Villas-Boas, Applied Phys. Lett. **93**, 052103 (2008).
[14]C. E. Pryor, and M. E. Pistol, Phys. Rev. B **72**, 205311 (2005).
[15]M. H. Degani and M. Z. Maialle, J. Comput. Theor. Nanosci. **7**, 454 (2010).
[16]M. D. Feit, J. A. Fleck, Jr., and A. Steiger, J. Comput. Phys. **47**, 412 (1982).
[17]M. H. Degani, Appl. Phys. Lett. **59**, 57 (1991), Phys. Rev. B **66**, 23306 (2002).
[18]M. Z. Maialle, M. H. Degani, J. R. Madureira, and P. F. Farinas, J. Appl. Phys. **106**, 123703 (2009).
[19]U. Fano and J. W. Cooper, Rev. Mod. Phys. **40**, 441 (1968).
[20]A. Tsolakidis, D. Sánchez-Portal, and R. M. Martin, Phys. Rev. B **66**, 235416 (2002).